

Citation for published version:
Gao, J, Ma, X, Chen, H, Zang, J & Dong, G 2021, 'On hydrodynamic characteristics of transient harbor resonance excited by double solitary waves', *Ocean Engineering*, vol. 219, 108345. https://doi.org/10.1016/j.oceaneng.2020.108345

10.1016/j.oceaneng.2020.108345

Publication date: 2021

Document Version Peer reviewed version

Link to publication

Publisher Rights CC BY-NC-ND

# **University of Bath**

## **Alternative formats**

If you require this document in an alternative format, please contact: openaccess@bath.ac.uk

**General rights** 

Copyright and moral rights for the publications made accessible in the public portal are retained by the authors and/or other copyright owners and it is a condition of accessing publications that users recognise and abide by the legal requirements associated with these rights.

If you believe that this document breaches copyright please contact us providing details, and we will remove access to the work immediately and investigate your claim.

Download date: 09. Mar. 2023

1	On hydrodynamic characteristics of transient harbor resonance excited by double
2	solitary waves
3	Junliang Gao <sup>1</sup> , Xiaozhou Ma <sup>2*</sup> , Hongzhou Chen <sup>3</sup> , Jun Zang <sup>4</sup> , Guohai Dong <sup>2</sup>
4	1. School of Naval Architecture and Ocean Engineering, Jiangsu University of Science and
5	Technology, Zhenjiang 212003, China.
6	2. State Key Laboratory of Coastal and Offshore Engineering, Dalian University of Technology,
7	Dalian 116024, China.
8	3. School of Civil Engineering and Architecture, Northeast Electric Power University, Jilin,
9	132012, China
10	4. Research Unit for Water, Environment and Infrastructure Resilience (WEIR), Department of
11	Architecture and Civil Engineering, University of Bath, BA2 7AY, U.K.
12	
13	Abstract:
14	The harbor resonance triggered by double solitary waves (DSWs) with different wave
15	parameters (including various wave heights and relative separation distances) is simulated based on
16	the fully nonlinear Boussinesq model, FUNWAVE-TVD. A long and narrow harbor with different
17	topographies is adopted. In the current study, effects of incident wave height, relative separation
18	distance and bottom profile on hydrodynamic characteristics related to the transient oscillations are
19	mainly investigated. The hydrodynamic characteristics considered include the evolution of the
20	maximum free-surface elevation, the maximum runup, the wave energy distribution and the total
21	wave energy inside the harbor. Results show that Green's law can accurately estimate the evolution
22	of the maximum free-surface elevation in most part of the harbor area. The impacts of the
23	topography on the maximum runup exhibit a strong dependence on the incident wave height. The
24	smaller mean water depth inside the harbor, the larger relative separation distance, and the higher
25	incident wave height tend to result in greater uniformity of the wave energy distribution. The
26	normalized total wave energy is always shown to decrease gradually with the incident wave height,
27	and to increase remarkably at first and then decrease slightly with the increase of the mean water

depth.

<sup>\*</sup>Corresponding author. E-mail: maxzh@dlut.edu.cn (X. Ma).

## **Key Words:**

- 2 Harbor resonance; Oscillations; Double solitary waves; Numerical simulation; Topographic effects;
- 3 FUNWAVE-TVD

## 1. Introduction

Harbor resonance is resulted from the gathering and magnification of incident wave energy at bays or harbors when the incident wave frequencies approach or equate to their eigenfrequencies (Gao et al., 2016a, 2020). Common triggering factors for the phenomenon include low-frequency waves, short wave groups, tsunamis, barometric variation, vessel-induced bores, local water-surface disturbance, and shear flow (Dong et al., 2013, 2020b; De Jong et al., 2003; Ma et al., 2020; Rupali et al., 2020; Fabrikant, 1995; Gao et al., 2017c, 2018b, 2018c, 2019c; Shao et al, 2020; Wang et al., 2020). Harbor oscillations has direct negative impacts on ship movement and port management. It can excite excessive movements of ships and unacceptable forces on mooring lines, and cause port operations poor efficient (Kumar et al., 2016).

Among the above-mentioned triggering factors, transient harbor resonance events excited by

Among the above-mentioned triggering factors, transient harbor resonance events excited by tsunamis have been often observed and many of them were devastating. As tsunamis travel into the coast, their wave heights usually rise dramatically owing to the persistent decline of the water depth. Take the Indian Ocean tsunami happening on December 26, 2004, for example. It was generated by the Sumatra earthquake and travelled for ~2 hours to Colombo Harbor in Sri Lanka, inducing remarkable resonance with the eigenperiod of ~1.25 hours and the maximum oscillation of ~3.9 m. It then travelled for ~14 hours to Bunbury Harbor in Australia, producing the maximum oscillation of ~1.8 m (Pattiaratchi and Wijeratne, 2009). Hence, to minimize both the interference to port operations and potential devastating impacts, further studies on hydrodynamic characteristics associated with harbor resonance are of vital importance to enhance related knowledge and thus improve our predictive ability.

Solitary waves have been widely adopted to represent real tsunamis in lots of studies due to the fact that some characteristics in real tsunami events, such as the persistent hump-like waveforms, can be imitated by solitary waves very well (e.g., Craig et al. (2006); Dong et al. (2020a); Hayatdavoodi et al. (2014); Liu et al. (1995); Seiffert et al. (2014); Synolakis (1987); Wang and Liu (2020)). However, based on some in-situ surveys which proved that the leading tsunamis was often

preceded by a depression, Tadepalli and Synolakis (1994) proposed the so called "N-waves" to represent tsunamis for the first time, and this type of tsunami waveform was further developed by Madsen and Schäffer (2010). Undular bores have also been frequently seen in the coast as tsunamis approach the shoreline (Madsen et al., 2008), and their evolutions in the coast can generate a train of multi-crested waves that are regarded as a train of solitary waves with various wave parameters (El et al., 2012; Grilli et al., 2012). The concept of double solitary waves (DSWs) was also proposed by a few scholars in the last few years (Dong et al., 2014; Lo et al., 2013).

The majority of the harbor-oscillation investigations triggered by tsunamis were performed via utilizing solitary waves or N-waves (e.g., Dong et al. (2010; 2020a); Gao et al. (2019a; 2019b)). On the other hand, the wave effects in the coast related to DSWs are basically confined to predicting their runup/backwash on beaches (e.g., Dong et al. (2014); Lo et al. (2013)). To the best of our knowledge, up to now, the studies of the transient harbor oscillations induced by DSWs are rare. Gao et al. (2018a) introduced DSWs for the first time to carry out the research on transient resonance inside an elongated harbor with a flat bottom, and the influences of various waveform parameters (including the incident wave height, the number of component solitary waves, and the relative separation distance between adjacent crests) on the relative wave energy distribution inside the harbor were investigated. Except Gao et al. (2018a), no more literature on the harbor resonance triggered by DSWs has been seen by the authors.

The present work also utilizes DSWs to further investigate the hydrodynamic characteristics associated with the transient oscillations. This article focuses on the impacts of different incident wave parameters and the bottom profile inside the harbor on various hydrodynamic characteristics during oscillations. The resonant hydrodynamics concerned include the evolution of the maximum free-surface elevation, the maximum runup, the wave energy distribution, and the total wave energy. It needs to be emphasized that it is of crucial importance to accurately estimate and comprehensively study these hydrodynamic characteristics. Both the evolution of the maximum free-surface elevation and the maximum runup are tightly correlated with the tsunami-triggered flood around the harbor area (e.g., Kumar and Gulshan (2017, 2018); Gao et al. (2016b; 2019b)); both the wave energy distribution and the total wave energy offer vital information for accurately predicting the movement of ships in harbors (Gulshan et al., 2020).

Compared with Gao et al. (2018a) where the transient harbor resonance triggered by DSWs

has been studied, the research progresses of this article are embodied in three respects. Firstly, Gao et al. (2018a) assumed the constant water depth inside the harbor. Nevertheless, for real harbors, their topographies are generally uneven (Gulshan et al., 2020; Kumar and Rupali, 2018). Therefore, in this article, more complicated bottom profiles are taken into consideration. Secondly, the wave heights of the DSWs adopted in Gao et al. (2018a) were relatively small; the wave condition was confined to the weak nonlinearity. On the contrary, the current study expands the wave fields in the harbor to the strong nonlinearity. Thirdly, the investigations on both the evolution of the total wave energy and the maximum free-surface elevation inside the harbor triggered by the DSWs are implemented in this article for the first time. In current research, all numerical cases are performed utilizing a fully nonlinear Boussinesq model. The harbor is assumed to be long and narrow; the motion of the free surface inside the harbor then substantially becomes one-dimensional (Gao et al., 2016c; Losada et al., 2008).

The remaining parts of this article is as follows. the numerical model and the data analysis methodology are first introduced in Section 2. Then, the setups associated with the numerical experiments are described in Section 3. Simulation results are analyzed and explained in Section 4. Main conclusions are summarized in Section 5.

## 2. Numerical model and data analysis methodology

#### 2.1. Numerical model

In the current study, all numerical experiments are performed utilizing the proverbial numerical model, FUNWAVE-TVD (Shi et al., 2012). The set of fully nonlinear Boussinesq equations proposed by Chen (2006) combined with a moving reference level are utilized as the control equations that are numerically discretized by using a hybrid finite-difference/finite-volume scheme. To carry out a high-order Total Variation Diminishing (TVD) scheme easily, the control equations are reorganized as in Ma et al. (2012) and Liu et al. (2020). To parallelize the numerical model, the Message Passing Interface (MPI) technique with non-blocking communication is introduced into the model as well. In addition, an adaptive time-stepping algorithm is adopted, which follows the Courant–Friedrichs–Lewy (CFL) criterion.

With these enhancements mentioned above, the numerical model becomes more robust and more powerful in predicting various hydrodynamic processes associated with water waves in the offshore and coastal areas. These processes include wave shoaling, diffraction, refraction, breaking, and wave runup/backwash on beaches (Liu et al., 2019; Ning et al., 2019b). To validate the capability of the numerical model in simulating the harbor resonance excited by transient long waves (e.g., tsunamis), the physical experiments of Dong et al. (2010) were fairly well reproduced in Gao et al. (2017a) by using FUNWAVE-TVD. It should be stressed in particular that the capacity of FUNWAVE-TVD to predict the wave profile evolution of tsunamis (e.g., solitary waves) over uneven topographies has been fully validated by Ning et al. (2019a) via comparing with experimental data, which ensures the correctness of the research results about the topographic influences on the harbor oscillations triggered by DSWs in this article.

## 2.2. Data analysis methodology

In order to acquire the total wave energy and the wave energy distribution for the harbor resonance excited by DSWs accurately, a data analysis methodology, namely, the normal mode decomposition (NMD) method, needs to be adopted.

The NMD method was developed by Sobey (2006) to estimate eigenmodes, eigenfrequencies, and response amplitudes of various modes for harbors suffered from tsunamis. The technique includes two calculation steps. In the 1<sup>st</sup> step, a series of eigenmodes and corresponding eigenfrequencies of the harbor are estimated. In the 2<sup>nd</sup> step, the prediction of the response amplitudes at various resonant modes are performed, which is expressed as a multi-dimensional optimization issue. Both the eigenmodes and the eigenfrequencies estimated in the former step are treated as known parameters in this process. Then, this technique was further ameliorated in Gao et al. (2015) to estimate eigenmodes and eigenfrequencies more precisely.

Based on the method, Gao et al. (2019a; 2019b) have comprehensively investigated the wave energy distribution aiming at the harbor resonance triggered by N-waves and solitary waves. For its detailed theory, the interested reader is referred to Gao et al. (2015) and Sobey (2006).

#### 3. Numerical setups

# 3.1. Incident wave parameters

If a solitary wave propagates along the *x*-axis over a flat bottom, its leading-order wave surface is expressed as follows (Mei, 1983):

$$\eta(x,t) = A_0 \operatorname{sech}^2 \left[ k(x-ct) \right], \tag{1}$$

2 where

3 
$$k = \sqrt{\frac{3A_0}{4h^3}}$$
, and  $c = \sqrt{g(A_0 + h)}$ . (2)

A<sub>0</sub> and c are the wave height and the traveling speed of the solitary wave, respectively, and h is the
 water depth.

Similar to Dong et al. (2014), in this article, the incident DSWs are created by the linear superposition of two component solitary waves with identical wave heights and different relative separation distances. Therefore, the incident DSWs adopted in all the numerical experiments can be formulated as

10 
$$\eta(x,t) = A_0 \left[ \operatorname{sec} h^2 \left( k \left( x - x_0 - ct - R \cdot L / 2 \right) \right) + \operatorname{sec} h^2 \left( k \left( x - x_0 - ct + R \cdot L / 2 \right) \right) \right], \tag{3}$$

where  $x_0$  is the central location of the initial waveform, and  $L=2\pi/k$  can be viewed as the effective wavelength of the component solitary wave. R, defined as the ratio of the distance between adjacent crests to L, is the so-called "relative separation distance". In FUNWAVE-TVD, the initial velocity of the incident DSWs takes a linear expression as following:

15 
$$u(x,t=0) = \sqrt{\frac{g}{h}}\eta(x,t=0). \tag{4}$$

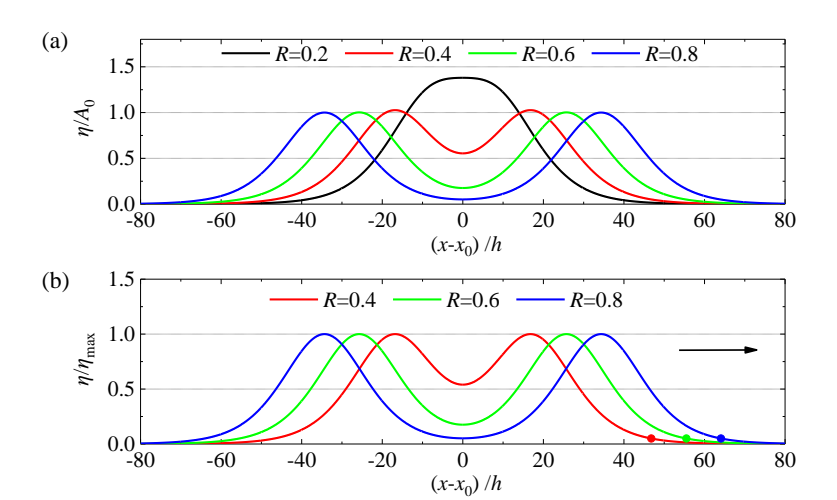


Fig. 1. Waveforms of the DSWs under conditions of  $A_0$ =0.100 m and h=14.0 m: (a) waveforms with R varying from 0.2 to 0.8 with an interval of 0.2; (b) the definition of the wavefront. The circle and the arrow in figure (b) indicate the wavefront and the direction of wave propagation, respectively.

For all the simulations considered in the present research, a constant water depth of 14.0 m is arranged outside the harbor. Fig. 1 presents the comparisons of the waveforms for the DSWs with  $A_0$ =0.100 m and various relative separation distances under the condition of h=14.0 m. It is seen that when R=0.2, the two component single waves fuse into one wave. As R rises to 0.4, there appear two distinctly-separated crests in the waveform, and their height,  $\eta_{\text{max}}$ , has already become extremely close to the wave height of the component solitary wave,  $A_0$ , that is,  $\eta_{\text{max}}$ =1.026 $A_0$ . Therefore, only the DSWs with  $R \ge 0.4$  are considered in this article.

**Table 1.** Incident wave parameters for DSWs and topographic parameters for the harbor

Group	Initial waveform	$A_0$ (m)	Type of topography	topographic parameters				
A		0.025,	are tangent type	$h_1$ =14 m, $h_0$ =4 m, $\alpha$ =6.8 m, $\bar{h}$ =12.43 m				
В	•	0.050,	arc-tangent-type	$h_1$ =14 m, $h_0$ =4 m, $\alpha$ =8.3 m, $\bar{h}$ =10.73 m				
С	DSWs with R=0.4	0.075, 0.1,	constant slope	$h_1=14 \text{ m}, h_0=4 \text{ m}, \overline{h}=9.00 \text{ m}$				
D	-	0.15, 0.2,	hymanhalia aasina tyma	$h_1$ =14 m, $h_0$ =4 m, $\kappa$ =0.15, $\bar{h}$ =7.69 m				
Е	•	0.25, 0.3	hyperbolic-cosine-type	$h_1$ =14 m, $h_0$ =4 m, $\kappa$ =200, $\bar{h}$ =6.54 m				
F		0.025,		$h_1$ =14 m, $h_0$ =4 m, $\alpha$ =6.8 m, $\bar{h}$ =12.43 m				
G		0.050, 0.075, 0.1,	arc-tangent-type	$h_1$ =14 m, $h_0$ =4 m, $\alpha$ =8.3 m, $\bar{h}$ =10.73 m				
Н	DSWs with R=0.6		constant slope	$h_1$ =14 m, $h_0$ =4 m, $\bar{h}$ =9.00 m				
I		0.15, 0.2,	hyperbolic-cosine-type	$h_1$ =14 m, $h_0$ =4 m, $\kappa$ =0.15, $\bar{h}$ =7.69 m				
J		0.25, 0.3	hyperbone-cosme-type	$h_1$ =14 m, $h_0$ =4 m, $\kappa$ =200, $\bar{h}$ =6.54 m				
K		0.025,	arc-tangent-type	$h_1$ =14 m, $h_0$ =4 m, $\alpha$ =6.8 m, $\bar{h}$ =12.43 m				
L	DSWs with <i>R</i> =0.8	0.050,	arc-tangent-type	$h_1$ =14 m, $h_0$ =4 m, $\alpha$ =8.3 m, $\bar{h}$ =10.73 m				
M		0.075, 0.1,	constant slope	$h_1=14 \text{ m}, h_0=4 \text{ m}, \bar{h}=9.00 \text{ m}$				
N		0.15, 0.2,	hyperbolic-cosine-type	$h_1$ =14 m, $h_0$ =4 m, $\kappa$ =0.15, $\bar{h}$ =7.69 m				
О		0.25, 0.3	nyperbone-cosme-type	$h_1=14 \text{ m}, h_0=4 \text{ m}, \kappa=200, \ \overline{h}=6.54 \text{ m}$				

The incident wave parameters for the DSWs utilized in all numerical experiments are listed in Table 1. Fifteen groups of numerical experiments (namely, Groups A-O) are taken into consideration, and each consists of eight cases with  $A_0$  varying from 0.025 m to 0.300 m to systematically investigate the effects of the wave height on the resonant hydrodynamic characteristics. The DSWs with R=0.4, 0.6, and 0.8 are used as the incident waves in Groups A-E, F-J, and K-O, respectively. The main purpose of designing Groups F-O lies in finding out how the relative separation distance affects the transient harbor oscillations triggered by DSWs.

In order to facilitate describing the setups of the NWT that will be shown in Subsection 3.2 and interpreting some research results that will be shown in Section 4, the concepts of "wavefront" and "wavelength" for the DSWs are defined here. The wavefront refers to the location at which the free-surface elevation equates to 0.05 times  $\eta_{\text{max}}$  (refer to Fig. 1b). In this paper, the wavelength of the DSWs,  $L_0$ , is defined as double the length between the wavefront and  $x_0$ . For the same  $A_0$ , the wavelength of the DSWs increases gradually with R. Table 2 further lists all the wavelengths of the incident DSWs with various wave heights and relative separation distances adopted in the present study. For the three waveforms of DSWs shown in Fig. 1b, their wavelengths gradually increase from 1310.2 m when R=0.4 to 1794.6 m when R=0.8. Besides, for the DSWs with the same relative separation distance, their wavelengths decrease gradually with the increase of  $A_0$ . Take the DSWs with R=0.4 for example. Their wavelengths decrease from 2620.0 m to 756.0 m as  $A_0$  rises from 0.025 m to 0.300 m.

**Table 2.** Wavelengths,  $L_0$ , of the DSWs with various relative separation distances and wave heights. The unit of the wavelength is meter.

$A_0$ (m)	0.025	0.050	0.075	0.100	0.150	0.200	0.250	0.300
$L_0$ when $R=0.4$	2620.0	1852.8	1512.6	1310.2	1069.8	926.4	828.6	756.0
$L_0$ when $R=0.6$	3108.0	2198.0	1794.2	1554.0	1268.8	1099.0	982.6	897.2
$L_0$ when $R=0.8$	3590.0	2538.0	2072.0	1794.6	1465.4	1269.0	1135.0	1036.2

Prior to performing the numerical experiments of the current study, it is necessary to check out the ability of the numerical model to generate DSWs. For this purpose, a simple numerical wave tank (NWT) is established (not shown in the paper). The NWT has a length of 8000 m, and the still water depth h for the whole computational domain is set to 14.0 m. The generated waves are set to propagate from left to right. The coordinate origin (i.e., x=0) is positioned at the left boundary. At the moment of t=0, the central location of the waveform is set to x0=2000 m. To record the incident wave train, a wave gauge is placed at x=4000 m. The uniform grid size of 1.0 m is adopted. The comparisons of the simulated and the analytical incident DSWs with x0=0.100 m and various relative separation distances are presented in Fig. 2. The incident DSWs generated by the model are shown to be in good agreement with the analytical ones.

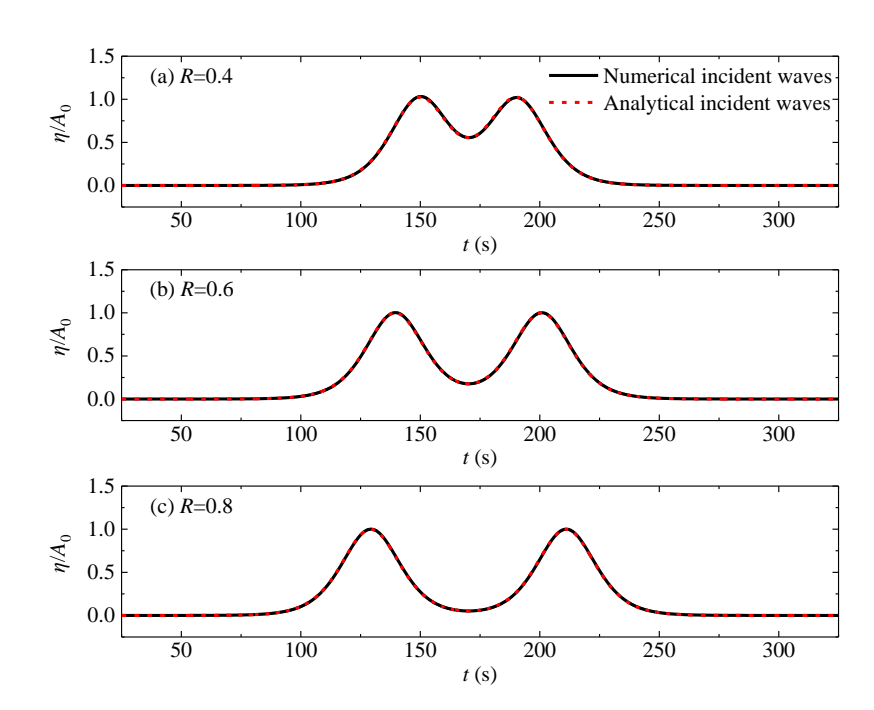


Fig. 2. Comparisons of the simulated and the analytical incident DSWs with  $A_0$ =0.100 m and various relative separation distances.

## 3.2. Numerical wave tank

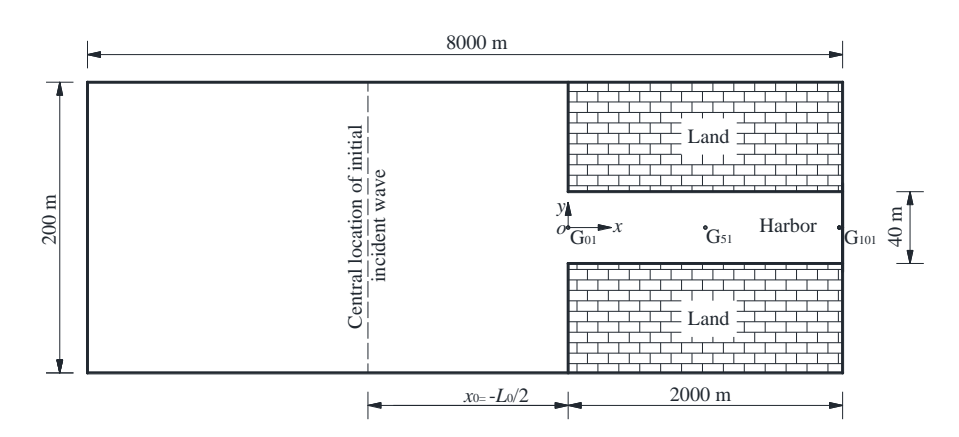


Fig. 3. Top view of the NWT used in all simulations.

Fig. 3 presents the NWT used in all simulations. The dimensions of the NWT and the harbor are 8000 m × 200 m and 2000 m × 40 m, respectively. All the boundaries are fully reflective. There are 101 wave gauges (i.e.,  $G_{01}$ – $G_{101}$ ) deployed along the central line of the harbor, and the space between any two adjacent gauges is 20 m.  $G_{01}$  is arranged at the harbor entrance (x=0), and  $G_{101}$  is at the backwall (x=2000 m). The water depth outside the harbor is set to a constant of  $h_1$ =14.0 m.

The grid sizes are uniform in 1 m along both the x- and the y-axes. As the initial condition, the wavefronts of the incident waves are always set to be located at the entrance (i.e.,  $x_0$  is always set to  $-L_0/2$ ) at the beginning of the simulation. The total simulation time for all cases is set to 800 s. In the adaptive time-stepping algorithm of FUNWAVE-TVD, one parameter C, termed as Courant number, needs to be presetted, which is set to 0.5 for all cases. The output time interval for the free-surface elevations at all gauges is set to 0.04 s.

To study the impacts of the topographic variation inside the harbor on the resonant hydrodynamic features induced by DSWs, three types of bottom profiles (including a hyperbolic-cosine-type bottom, a plane slope bottom, and an arc-tangent-type bottom) are adopted in this paper. The water depth inside the harbor,  $h_d(x)$ , is formulated as (Gao et al., 2017b):

11 
$$h_{\rm d}(x) = \begin{cases} h_0 \cosh^{\kappa} \left[ \mu(L - x) \right] & \text{hyperbolic-cosine-type bottom} \\ h_1 - \gamma x & \text{constant-slope bottom} \\ h_0 + \alpha \arctan \left[ \beta(L - x) \right] & \text{arc-tangent-type bottom} \end{cases} , \tag{5}$$

where  $h_0$  denotes the water depth at the backwall and is set to 4.0 m.  $\alpha$ ,  $\beta$ ,  $\gamma$ ,  $\kappa$  and  $\mu$  are topographical parameters, and comply with the following relationships:

14 
$$\beta = \frac{1}{L} \tan\left(\frac{h_1 - h_0}{\alpha}\right), \gamma = \frac{h_1 - h_0}{L}, \text{ and } \mu = \frac{1}{L} \operatorname{acosh}\left[\left(\frac{h_1}{h_0}\right)^{1/\kappa}\right].$$
 (6)

The types of the bottom profiles and the values of the topographic parameters used in all groups are also presented in Table 1. In this table,

$$\bar{h} = \frac{1}{b} \int_0^L h^{\mathrm{I}}(x) dx \,, \tag{7}$$

which denotes the mean water depth inside the whole harbor.

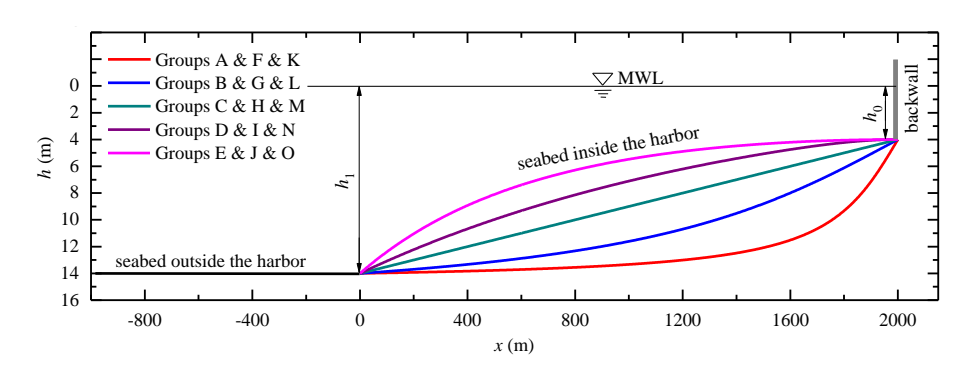


Fig. 4. Comparisons of various topographies inside the harbor

Fig. 4 illustrates all the five topographies adopted in the present study. The harbor utilized in

Groups A, F, and K has the arc-tangent-type topography, and the mean water depth  $\bar{h}$  is 12.43 m. The harbor in Groups B, G and L has the arc-tangent-type bottom profile as well. Nevertheless,  $\bar{h}$  declines to 10.73 m due to a larger magnitude of  $\alpha$ . The harbor in Groups D, I, and N has the hyperbolic-cosine-type topography, and  $\bar{h}$  is 7.69 m. Because of the increased  $\kappa$ ,  $\bar{h}$  in Groups E, J, and O decreases to 6.54 m. The harbor in Groups C, H, and M has a constant-slope bottom, and has  $\bar{h}$ =9.00 m.



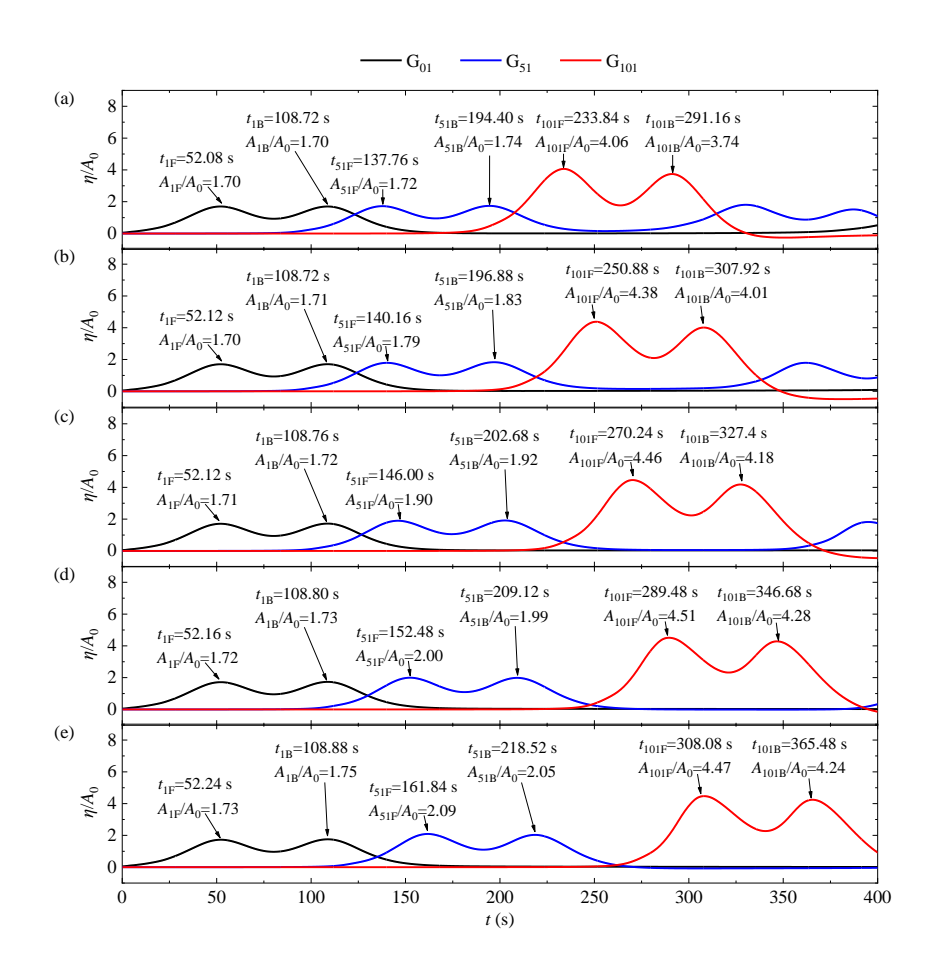


Fig. 5. Time histories of the free-surface elevations at various wave gauges under conditions of  $A_0$ =0.050 m and R=0.4. (a)-(e) correspond to Groups A-E, respectively.

## 4. Results and discussion

## 4.1. Time histories of free-surface elevations

Fig. 5 illustrates the time histories of the free-surface elevations at gauges  $G_{01}$ ,  $G_{51}$ , and  $G_{101}$  for the five cases with  $A_0$ =0.050 m and R=0.4 in Groups A-E.  $A_{iF}$  and  $A_{iB}$  in the figure respectively denote the wave-crest elevations of the front and the back component solitary waves at

the  $i^{th}$  gauge. The five cases have the same incident waves but various bottom profiles (refer to Table 1). Three phenomena can be seen from the figure. Firstly, for all these cases, the wave-crest elevations of the front component solitary waves at gauges  $G_{01}$  and  $G_{51}$  are almost equal to the corresponding ones of the back component solitary waves. However, for gauge  $G_{101}$ , the value of  $A_{101F}$  becomes remarkably larger than that of  $A_{101B}$ . Secondly, because the local water depth declines continuously as the incident DSWs travel from the entrance to the backwall, the maximum elevations at all the three gauges increase gradually. Thirdly, the wave-crest elevations at gauges  $G_{51}$  and  $G_{101}$  gradually rise with the decline of the mean water depth inside the harbor, overall. It can be attributed to the fact that the smaller mean water depth leads to the more obvious shoaling effect (i.e., the more remarkable wave height amplification).

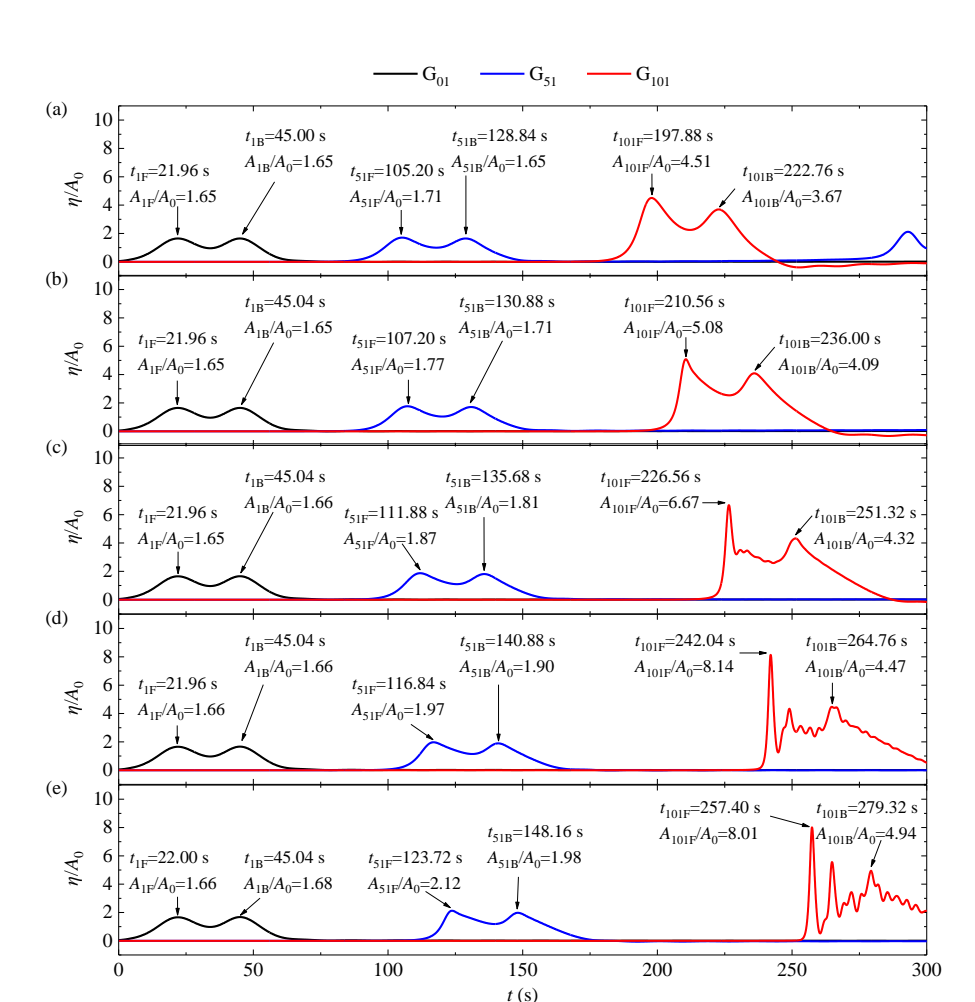


Fig. 6. Time histories of the free-surface elevations at various wave gauges under conditions of  $A_0$ =0.3 m and R=0.4. (a)-(e) correspond to Groups A-E, respectively.

Fig. 6 further demonstrates the time histories of the free-surface elevations at gauges G<sub>01</sub>, G<sub>51</sub>,

and  $G_{101}$  for the five cases with  $A_0$ =0.300 m and R=0.4 in Groups A-E. Compared to Fig. 5, some different phenomena appear. Although the wave-crest elevations of the front component solitary wave still keep almost identical to the ones of the back component solitary wave at gauge  $G_{01}$ , the former becomes notably larger than the latter at gauge  $G_{51}$ . In addition, because of the larger incident wave height, the free-surface elevations at gauges  $G_{51}$  and  $G_{101}$  present remarkable wave nonlinearity, which is specifically embodied in two respects. Firstly, apparent asymmetry can be seen in the front component solitary wave at gauges  $G_{51}$  and  $G_{101}$ . For the front component solitary waves at gauge  $G_{101}$  in Fig. 6a and b and that at gauges  $G_{51}$  in Fig. 6e, their free surfaces rise promptly from zero to the maximum elevations, while their paces of decline are much slower. Secondly, for gauge  $G_{101}$  shown in Fig. 6c-e, except the two wave crests generated directly by the incident DSWs, there still exist one or more secondary peaks between the two wave crests. In general, the smaller mean water depth inside the harbor and the larger incident wave height lead to the more significant wave nonlinearity.

#### 4.2. Evolution of the maximum free-surface elevation

Considering that the maximum free-surface elevation is tightly related to the tsunami-triggered flood around the harbor area, its evolution inside the harbor is comprehensively investigated in this subsection as the incident DSWs propagates from the harbor entrance to the backwall. Via reading the time histories of the free surfaces at all gauges, the maximum elevation evolution inside the harbor can be directly acquired. Fig. 7 illustrates the evolution of the maximum free-surface elevation for Groups A, F and K under different incident wave heights. The three groups have the maximum mean water depth inside the harbor, 12.43 m. Because the local water depth continuously decreases as the incident DSWs travel to the backwall, the maximum free-surface elevation gradually increases as expected, except at the area where the incident and the reflected waves interact with each other near the backwall. Based on the linear wave theory and the assumption that the wave energy due to the reflection is neglected, the wave height of the long waves travelling over mild slopes can be estimated theoretically using Green's law (Mei, 1983):

$$\frac{A}{A_{\Delta}} = \left(\frac{h_{\Delta}}{h}\right)^{1/4},\tag{8}$$

where  $A_{\Delta}$  refers to the wave height at a certain reference position, and  $h_{\Delta}$  refers to the local water depth there. The evolution of the maximum free-surface elevation estimated by Green's law is

presented in this figure. It is noted here that the reference position for the calculation of Eq. (8) is set at gauge  $G_{02}$  rather than at gauge  $G_{01}$  to remove the boundary effect caused by the harbor entrance.

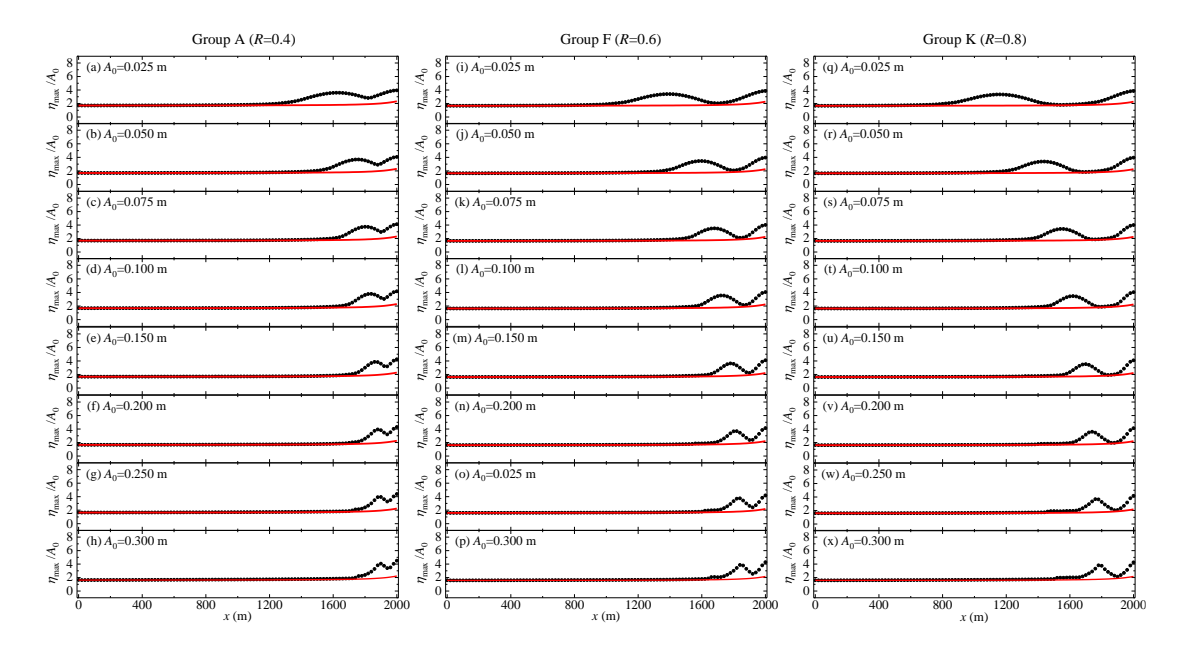


**Fig. 7.** Evolutions of the maximum free-surface elevations for Groups A, F and K. Black dots and red curves denotes the maximum free-surface elevations obtained directly by the simulations and those predicted by Green's law, respectively.

It is seen from this figure that for all these cases, Green's law predicts the numerical results very well inside the whole harbor except at the area where the incident and the reflected waves interact with each other near the backwall. In addition, it can be easily observed that for a given value of R, the spatial range where Green's law is valid gradually increases with the increase of the incident wave height. Similarly, it can be found that for a given value of  $A_0$ , the valid spatial range of Green's law also increases gradually with the decrease of R, no matter whether  $A_0$  is large or small. They are because the interaction area of the incident and the reflected waves contracts gradually as  $A_0$  increases and as R decreases, which coincides with the dependency of the incident wavelength on these two parameters (refer to Table 2).

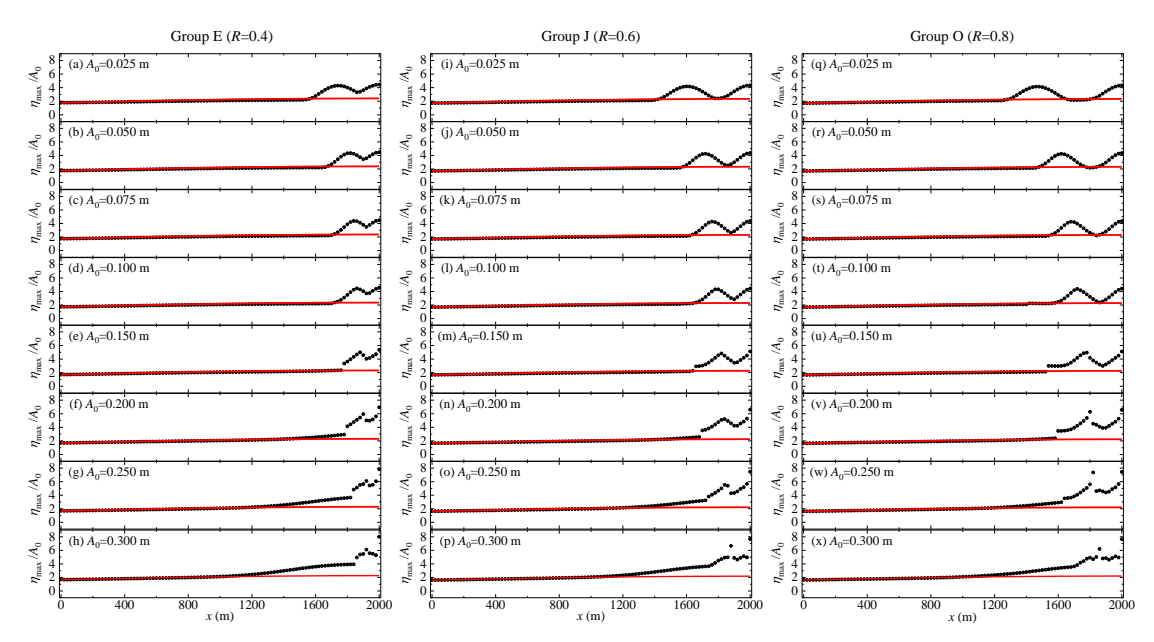


**Fig. 8.** Evolutions of the maximum free-surface elevations for Groups E, J and O. The meanings of black dots and red curves are identical to those in Fig. 7.

Fig. 8 further shows the evolution of the maximum free-surface elevation for Groups E, J and O under various incident wave heights. Different from Fig. 7, all three groups in this figure have the smallest mean water depth, 6.54 m. Similar to Fig. 7, Green's law is also shown to predict the maximum elevation accurately in most part of the harbor except at the small area around the backwall, and its valid spatial range increases gradually with the decline of R as well.

However, because of the decline of the mean water depth, a different phenomenon can be observed from Fig. 8. As the incident wave height increases, the valid spatial range of Green's law does not monotonically increase any more. Instead, the valid spatial range of Green's law becomes to first increase and then remarkably decrease with the rise of the incident wave height, which can be attributed to the secondary peak phenomenon shown in Fig. 6. As mentioned above, the larger incident wave height and the smaller mean water depth tend to cause the more significant wave nonlinearity (including the occurrence of the secondary peak phenomenon). The secondary peak can result in the narrower spatial span of the front wave crest, and the wave energy there becomes more concentrated. Hence, it results in the remarkable increase of the maximum free-surface elevation there. Through examining the free-surface elevations in these cases (the related results are not shown here), it is found that the secondary peak phenomenon begins to appear when  $A_0$ =0.150 m and becomes more and more evident as  $A_0$  further increases. It is accordance with the phenomenon

in Fig. 8 that the valid spatial range of Green's law increases notably as  $A_0$  rises from 0.150 m to 0.300 m.

#### 4.3. Maximum runup

Observing Figs. 7 and 8 can find that the maximum runup of the incident DSWs always occurs at the backwall, no matter whether the mean water depth, the relative separation distance, and the incident wave height are large or small. Fig. 9 shows the normalized maximum runups,  $A_{\rm u}/h_0$ , for the three topographies with  $\bar{h}$  =12.43 m, 9.00 m, and 6.54 m. Two apparent phenomena can be seen from the figure. Firstly, the maximum runups caused by the incident DSWs with the same incident wave height and various relative separation distances are almost identical to each other when  $A_0 \le 0.150$  m for all these three topographies. However, as  $A_0$  further increases, the maximum runups with R=0.4 gradually becomes larger than those with R=0.6 and 0.8. The maximum runups with R=0.6 are still almost identical to those with R=0.8, regardless of the bottom profile inside the harbor and the incident wave height.

Secondly, although the maximum runups increase monotonously with the increase of  $A_0$  for all these three topographies at the variation range of  $A_0$  considered, their growth characteristics closely depends on the topography. For the topography with  $\bar{h}$  =12.43 m (Fig. 9a), the maximum runup seems to always increase linearly with  $A_0$ . For the topography with  $\bar{h}$  =9.00 m (Fig. 9b), the increasing rate of  $A_0$  seems to remain unchanged when  $A_0 \le 0.150$  m and then rises gradually as  $A_0$  increases further. While for the topography with  $\bar{h}$  =6.54 m (Fig. 9c), the increasing rate of  $A_0$  first remains unchanged when  $A_0 \le 0.100$  m, then increases, and then decreases with the increase of  $A_0$ .

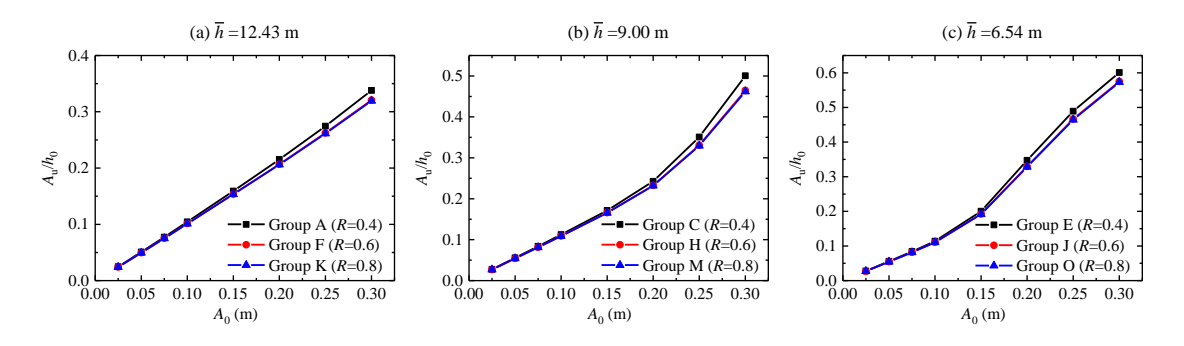


**Fig. 9.** The normalized maximum runups,  $A_u/h_0$ , for the three topographies with (a)  $\bar{h} = 12.43$  m, (b)

 $\bar{h} = 9.00 \text{ m}$ , and (c)  $\bar{h} = 6.54 \text{ m}$ .



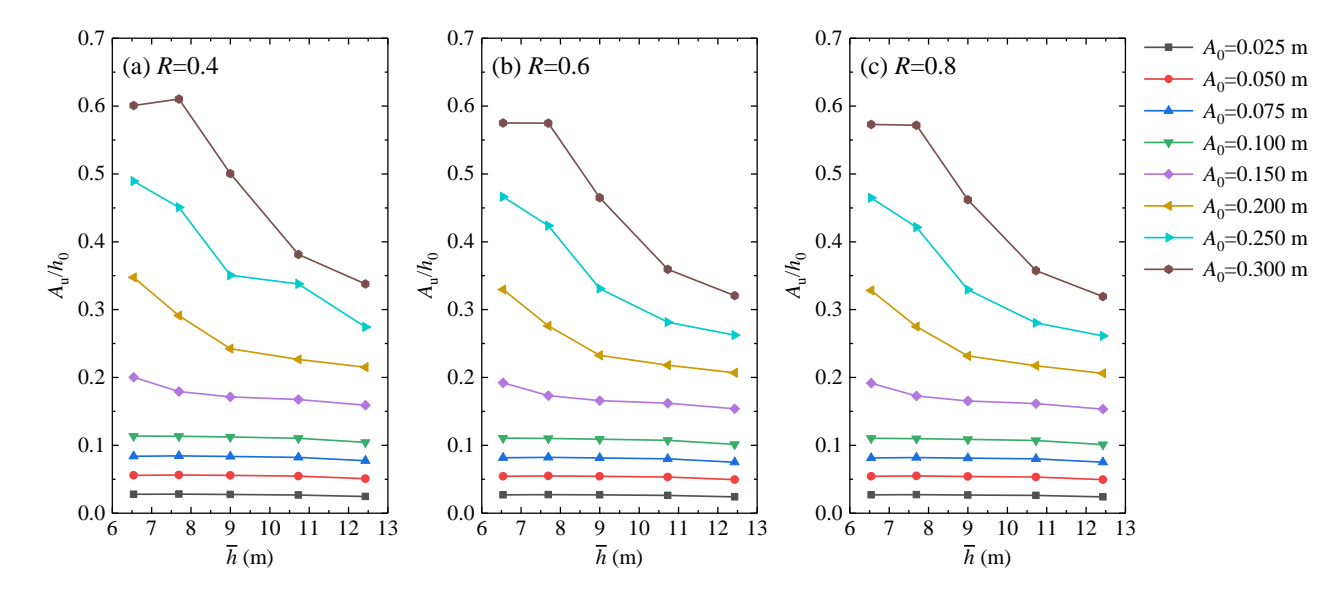


Fig. 10. Variations of the maximum runups with respect to the mean water depth induced by the DSWs with different values of R.

To better explain the impacts of the topography on the maximum runup, Fig. 10 illustrates the variations of the maximum runups with respect to the mean water depth subjected to the incident DSWs with different values of R. It is seen that when  $A_0 \le 0.100$  m, the topographic variation inside the harbor has very little effect on the maximum runup. Nevertheless, as  $A_0$  further increases, the effects of the topographic variation on the maximum runup relies heavily on both the relative separation distance and the incident wave height. For the incident DSWs with R=0.4 (Fig. 10a), when  $0.100 \text{ m} \le A_0 \le 0.250 \text{ m}$ , the maximum runup decreases monotonously with the increase of  $\bar{h}$ . As  $A_0$  increases to 0.300 m, the maximum runup becomes to first increase slightly, and then decrease sharply with the rise of  $\bar{h}$ . While for the incident DSWs with R=0.6 and 0.8 (Fig. 10b and c), the maximum runup always declines monotonously with the increase of  $\bar{h}$  when  $A_0$  is at the range of 0.100 m – 0.300 m.

- 4.4. Wave energy distribution and total wave energy
- 20 4.4.1. Computing process for the response amplitudes of various resonant modes
  - This subsection presents the detailed computing process of the NMD method for extracting the

response amplitudes of various modes from the wave fields inside the whole harbor. The time histories of the free-surface elevations at gauge  $G_{01}$  for the three cases with  $A_0$ =0.075 m in Groups A, F and K are illustrated in Fig. 11. Only the wave fields inside the harbor from  $t_0$  to  $t_1$  are adopted to calculate the response amplitudes of various modes.  $t_0$  and  $t_1$  denote the moment that the incident DSWs totally travel into the harbor and the moment that the reflected DSWs from the backwall begin to travel away from the entrance, respectively. Because the incident DSWs in these three cases have different relative separation distances and hence different wavelengths (refer to Table 2), the values of both  $t_0$  and  $t_1$  are different from each other. As R increases from 0.4 to 0.8, the value of  $t_0$  increases gradually from 170 s to 200 s, and that of  $t_1$  rises gradually from 320 s to 350 s.



9

1

2

3

4

5

6

7

8

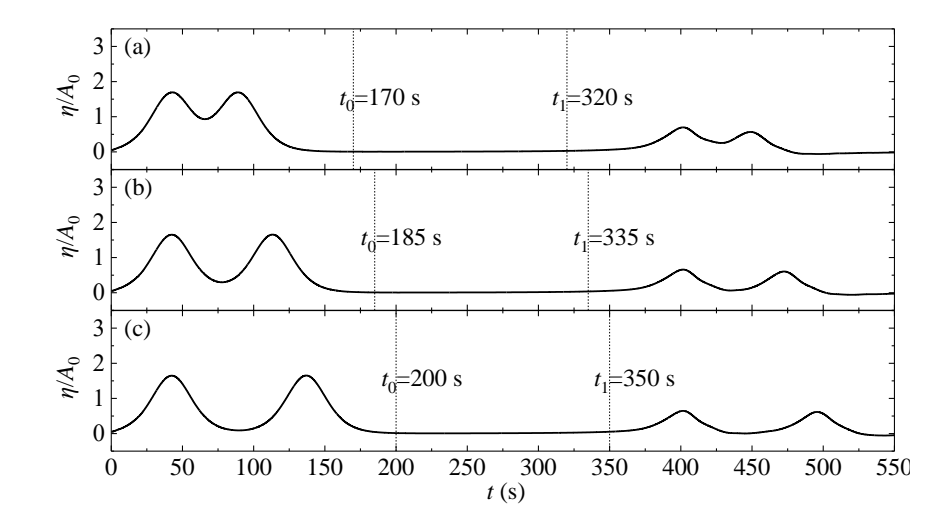


Fig. 11. Time histories of the free-surface elevations at gauge  $G_{01}$  for the three cases with  $A_0$ =0.075 m in (a) Group A, (b) Group F, and (c) Group K.

14 15

11

12

13

17

18

16

19 20

21 22

23

(a) Fitted curved surface Simulated curved surface  $\eta$  (m) η (m) 320 320 0.3 0.3 x: 2000 m x: 2000 m t: 271.00 s t: 271.00 s 280 280 А101В: 0.2819 m А101B: 0.2820 m 0.2 0.2 ② 240 ② 240 x: 2000 m x: 2000 m 0.1 t: 223.80 s t: 223.80 s

Fig. 12. Comparisons of the simulated and the fitted wave fields for the three cases with  $A_0=0.075$ m in (a) Group A, (b) Group F, and (c) Group K. Fig. 12 demonstrates the comparisons of the simulated and the fitted wave fields for the three cases presented in Fig. 11. The simulated wave field is directly acquired via the numerical simulations, and the fitted one is obtained by the NMD method. Good agreement between them is observed for all the three cases. Take the case with  $A_0$ =0.075 m in Group A for example (Fig. 12a). The simulated wave field has two maximum runups at x=2000 m. The first one has a value of  $A_{101F}$ =0.3092 m at t=223.80 s, and the second one is  $A_{101B}$ =0.2819 m at t=271.00 s. At the identical positions and moments, the fitted wave field has the first and the second maximum runups of 0.3088 m and 0.2820 m, respectively. To assess the fitting accuracy quantitatively, the numerical fitting error (NFE) of the NMD

method is defined here (Gao et al., 2018a):

1 
$$NFE = \max \left\{ \frac{\left| \left( A_{101F} \right)_{\text{fitted}} - A_{101F} \right|}{A_{101F}}, \frac{\left| \left( A_{101B} \right)_{\text{fitted}} - A_{101B} \right|}{A_{101B}} \right\} \times 100\% , \qquad (9)$$

where  $(A_{101F})_{\text{fitted}}$  and  $(A_{101B})_{\text{fitted}}$  respectively denote the fitted first maximum runup and the fitted second one at the backwall. The *NFE*s for the three cases in Fig. 12a–c are 0.13%, 0.10% and 0.14%, respectively. Table 3 further presents the *NFE*s for all the cases with  $A_0$  ranging from 0.025 m to 0.100 m. It is seen that the *NFE*s for these cases are all less than 5.00%. It indicates that the data analysis methodology estimates the response amplitudes of different modes accurately. The estimated response amplitudes for these cases will be presented in Subsection 4.4.2.

**Table 3.** Numerical fitting errors (*NFE*s) of the NMD method for all the cases with  $A_0$ =0.025 m, 0.050 m, 0.075 m, and 0.100 m. The unit of the *NFE* is %.

$A_0$	Group														
(m)	A	В	C	D	Е	F	G	Н	I	J	K	L	M	N	О
0.025	0.14	0.05	0.18	0.17	0.38	0.12	0.11	0.18	0.10	0.28	0.10	0.13	0.38	0.20	0.19
0.050	0.16	0.32	0.72	1.37	2.24	0.31	0.14	0.74	1.32	2.29	0.26	0.20	0.65	1.23	1.79
0.075	0.13	0.85	1.99	2.65	3.24	0.10	0.72	1.78	3.07	3.70	0.14	0.75	1.75	2.83	4.32
0.100	0.53	2.24	2.61	3.50	4.44	0.29	2.10	2.96	4.53	4.70	0.39	1.86	4.00	4.80	4.98

## 4.4.2. Wave energy distribution

To better show the wave energy distribution inside the harbor, the response amplitude of each mode is normalized by that of the corresponding first mode, i.e.,

15 
$$\bar{A}_i = \frac{A_i}{A_1} \quad (i = 1, 2, ..., 40),$$
 (10)

in which  $A_i$  denotes the response amplitude of the  $i^{th}$  mode, and the normalized response amplitude,  $\overline{A}_i$ , is referred to as "relative amplitude" hereinafter.

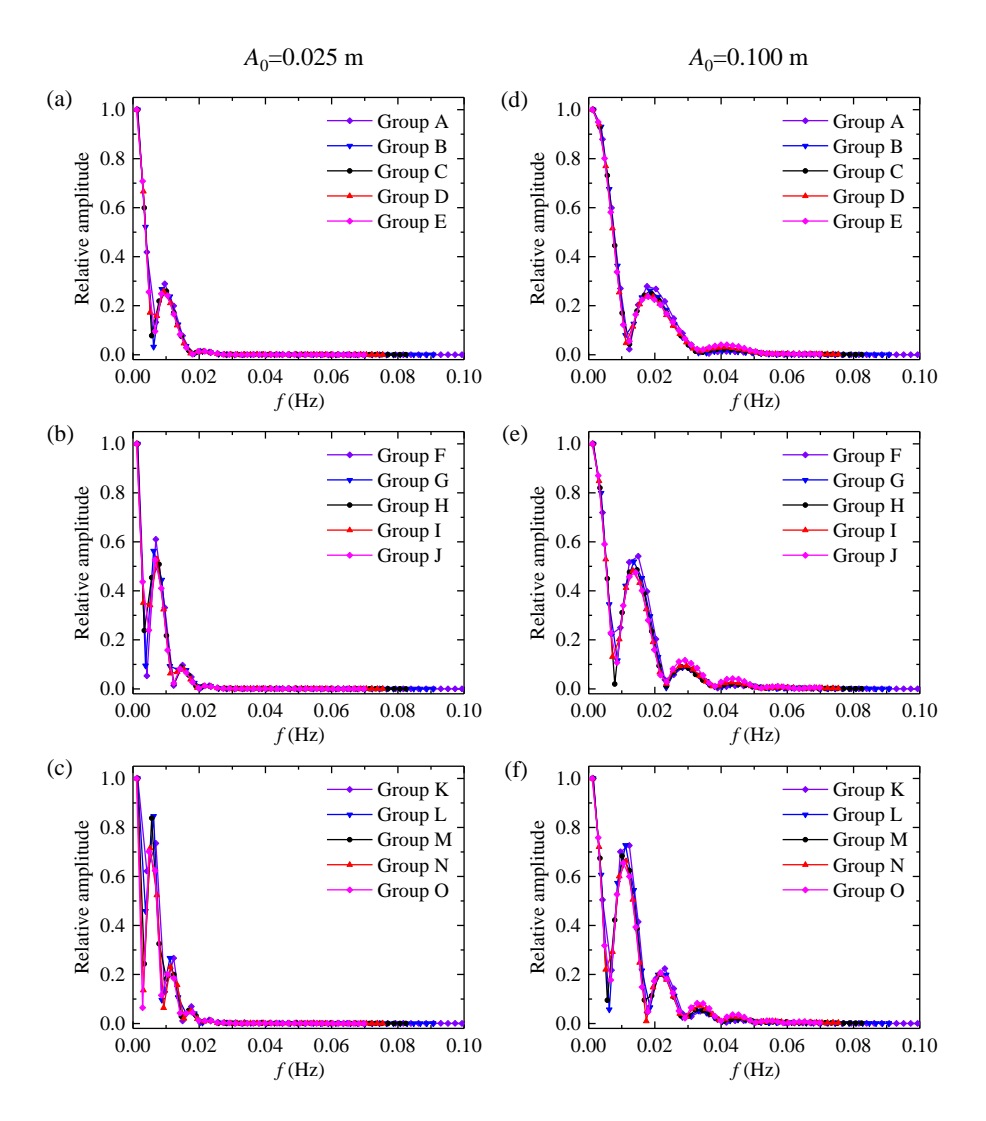


**Fig. 13**. Relative amplitudes of the lowest 40 modes inside the harbor with different topographies. (a)-(c) correspond to the incident DSWs with R=0.4, 0.6, and 0.8 for  $A_0$ =0.025 m, respectively; (d)-(f) correspond to the incident DSWs with R=0.4, 0.6, and 0.8 for  $A_0$ =0.100 m, respectively.

Fig. 13 presents the relative amplitudes of the lowest 40 modes inside the harbor with different topographies when  $A_0$ =0.025 m and 0.100 m. Three apparent phenomena can be observed. Firstly, for all these cases, the first resonant mode always has the largest response amplitude. Secondly, the relative wave energy distribution is shown to become more uniform for the larger incident DSWs. Take the cases with R=0.4 for example. When the incident wave height is small (i.e.,  $A_0$ =0.025 m) (Fig. 13a), the wave energy is dominated by the lowest few modes. As the incident wave height rises to  $A_0$ =0.100 m (Fig. 13d), the proportion of the wave energy occupied by the higher modes is shown to increase notably. This phenomenon can also be observed for the cases with R=0.6 (Fig. 13b and

e) and with R=0.8 (Fig. 13c and f). Thirdly, the larger relative separation distance also tends to result in the greater uniformity of the wave energy distribution, which can be easily seen via comparing the relative-amplitude curves in Fig. 13a–c or those in Fig. 13d–f.

Although the influences of both the relative separation distance and the incident wave height on the wave energy distribution can be observed relatively easily, it seems difficult to directly reveal from Fig. 13 how the variation of the bottom profile influences the wave energy distribution. To measure the uniformity of the energy distribution quantitatively, the coefficient of variance (CV) of the response amplitudes of various modes is utilized in the current study. CV is defined as

$$CV = \frac{\sigma}{\mu},\tag{11}$$

10 where

11 
$$\sigma = \sqrt{\frac{1}{40} \sum_{i=1}^{40} (A_i - \mu)^2}, \qquad (12)$$

12 and

13 
$$\mu = \frac{1}{40} \sum_{i=1}^{40} A_i \ . \tag{13}$$

Apparently, CV directly reflects the deviation degree of these response amplitudes from their average value; the lower CV indicates the greater uniformity of the energy distribution.

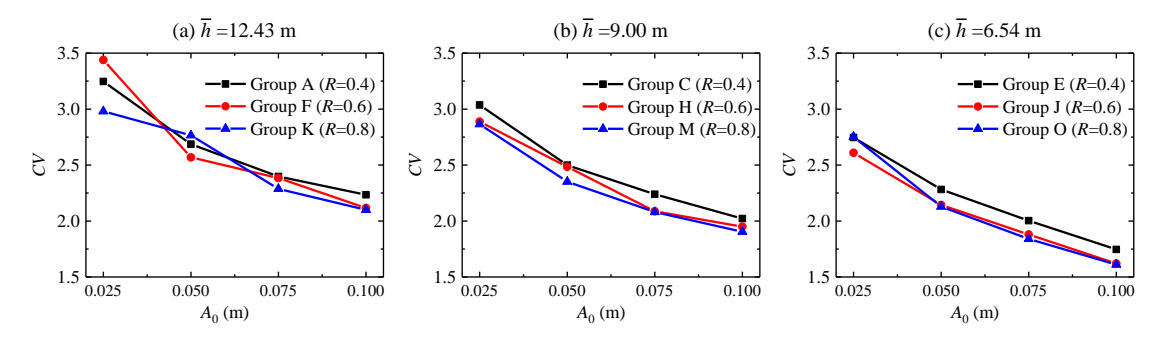
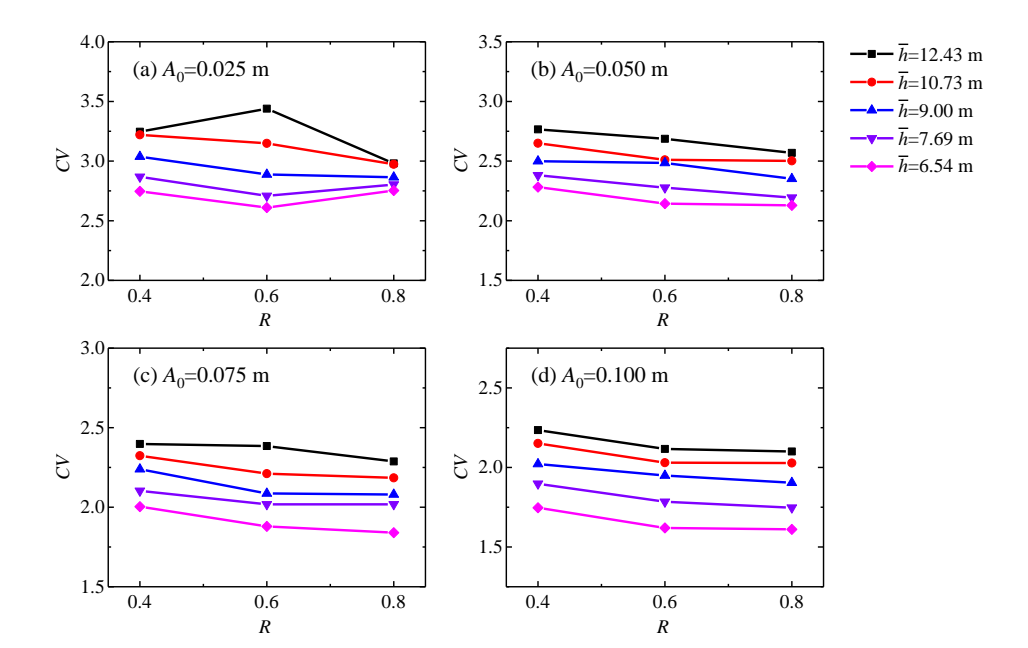


Fig. 14. Variations of the CV value with respect to  $A_0$  for the three topographies with (a)  $\bar{h} = 12.43 \text{ m}$ , (b)  $\bar{h} = 9.00 \text{ m}$ , and (c)  $\bar{h} = 6.54 \text{ m}$ .

Fig. 14 demonstrates the variation of the CV value with respect to  $A_0$  for the three topographies with  $\bar{h}$  =12.43 m, 9.00 m, and 6.54 m. For all the three topographies and all the relative separation

distances, CV always monotonously decreases with the increase of  $A_0$ , which indicates that the energy distribution inside the harbor has the greater uniformity as the incident wave height rises. In fact, the similar tendency can also be observed for the other two topographies (i.e.,  $\bar{h} = 10.73$  m and 7.69 m), and their related results are not presented here.





**Fig. 15.** Variations of the CV value with respect to R under various incident wave heights.

Fig. 15 shows the variations of the CV value with respect to R for various incident wave heights. The third phenomenon intuitively observed in Fig. 13 is further proved by this figure. For all the topographies considered, CV always gradually decreases with the rise of R when  $A_0$ =0.050 m, 0.075 m and 0.100 m (Fig. 15b–d). When  $A_0$ =0.025 m (Fig. 15a), this tendency is also observed for the bottom profiles with  $\overline{h}$  =10.73 m and 9.00 m.

Fig. 16 further presents the variation of *CV* with respect to the mean water depth for the incident DSWs with various relative separation distances. For all the relative separation distances considered, the *CV* values always decrease monotonously with the decrease of the mean water depth, regardless of the incident wave height. This indicates that the smaller mean water depth can result in the greater uniformity of the wave energy distribution, no matter whether the relative separation distance and the incident wave height are large or small.

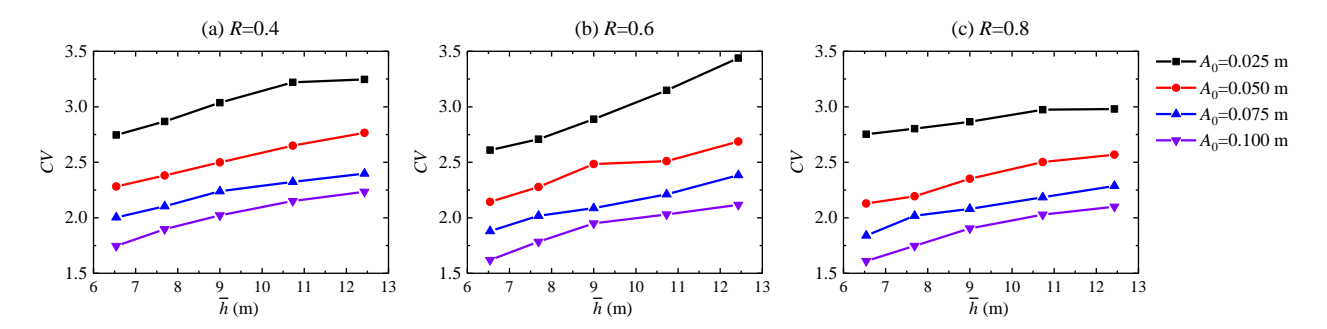


**Fig. 16.** Variations of the CV value with respect to  $\bar{h}$  for the incident DSWs with (a) R=0.4, (b)

3 R=0.6, and (c) R=0.8.

1

2

4

6

9

12

5 4.4.3. Total wave energy

The total wave energy inside the harbor can be accurately calculated as

$$E = \sum_{i=1}^{40} \frac{1}{2} A_i^2 \,, \tag{14}$$

8 according to the fact that the total wave field inside the harbor is a linear superposition of various

modes (Sobey, 2006). In this subsection, the normalized total wave energy defined as

$$\overline{E} = E/(0.5A_0^2) \tag{15}$$

is investigated.

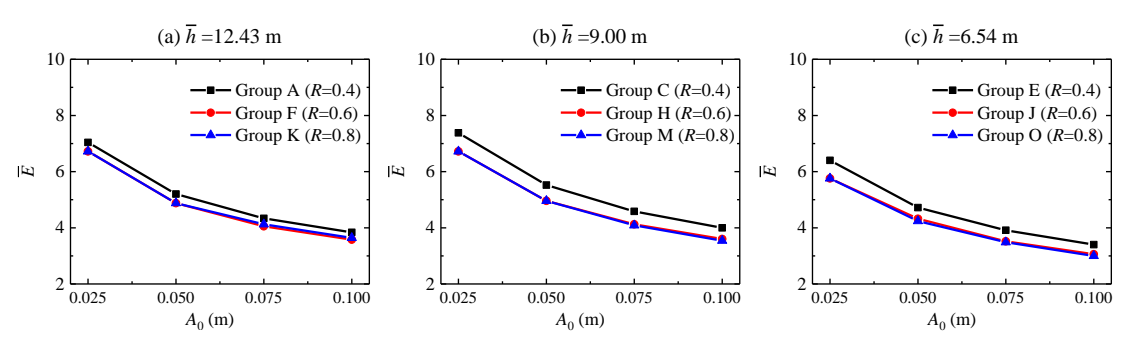


Fig. 17. Variation of the normalized total wave energy with respect to  $A_0$  for the three topographies

15 with (a)  $\bar{h} = 12.43 \text{ m}$ , (b)  $\bar{h} = 9.00 \text{ m}$ , and (c)  $\bar{h} = 6.54 \text{ m}$ .

16

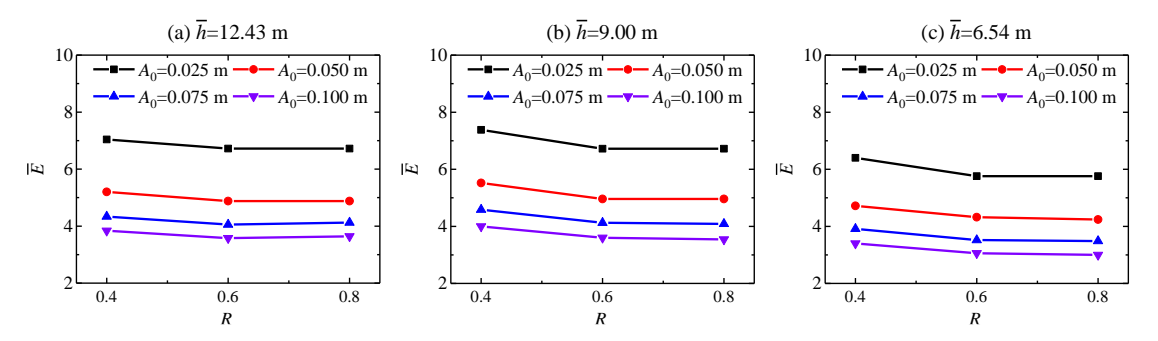
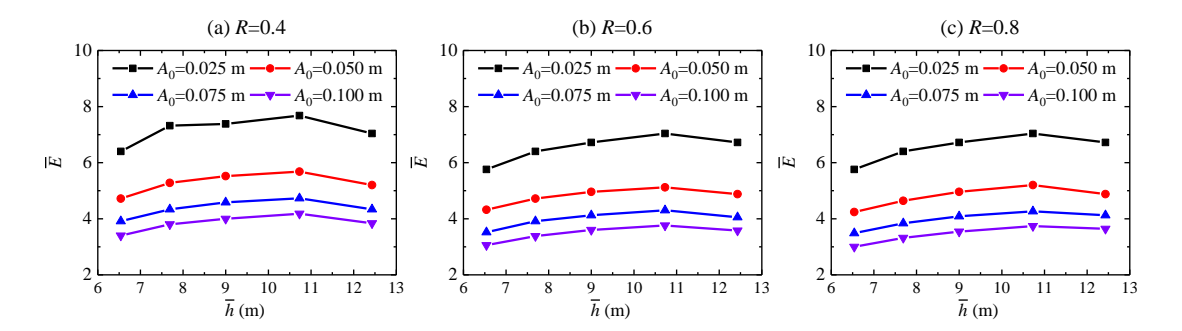


Fig. 18. Variation of the normalized total wave energy with respect to R for the three topographies with (a)  $\bar{h} = 12.43 \text{ m}$ , (b)  $\bar{h} = 9.00 \text{ m}$ , and (c)  $\bar{h} = 6.54 \text{ m}$ .

Fig. 17 shows the variation of the normalized total wave energy with respect to  $A_0$  for the three topographies with  $\bar{h}$  =12.43 m, 9.00 m, and 6.54 m. There are two apparent phenomena that can be easily seen. Firstly, for all these topographies, the normalized total wave energy decreases monotonously with the rise of the incident wave height, no matter whether R is large or small. Secondly, the normalized total wave energy triggered by the DSWs with R=0.4 is always larger than that excited by the DSWs with R=0.6 and 0.8 at the variation range of  $A_0$  considered. Besides, the normalized total wave energy with R=0.6 is shown to be always extremely close to that with R=0.8. To present the second phenomenon more intuitively, the variation of the normalized total wave energy with respect to R for the three topographies are further demonstrated in Fig. 18. It shows that when R rises from 0.4 to 0.6, the normalized total wave energy presents a certain degree of decline, while as R grows further from 0.6 to 0.8, the normalized total wave energy becomes insensitive to R. Similar phenomena to those in Figs. 17 and 18 can also be easily observed for the other two topographies (i.e.,  $\bar{h}$  =10.73 m and 7.69 m).

Fig. 19 further demonstrates the variation of the normalized total wave energy with respect to the mean water depth under conditions of various relative separation distances and incident wave heights. As the mean water depth increases from 6.54 m to 10.73 m, the normalized total wave energy always presents a continuous rise. While as the mean water depth rises further to 12.43 m, the normalized total wave energy shows a slight decrease, no matter whether the relative separation distances and the incident wave heights are large or small. The maximum total wave energy always occurs on the topography with  $\bar{h} = 10.73$  m.



**Fig. 19.** Variation of the normalized total wave energy with respect to  $\bar{h}$  for the incident DSWs with (a) R=0.4, (b) R=0.6, and (c) R=0.8.

#### 5. Conclusions

In the present study, the transient harbor resonance inside a long and narrow harbor with various bottom profiles triggered by DSWs with different relative separation distances and wave heights are simulated by adopting the FUNWAVE-TVD model. Influences of the incident wave height, the relative separation distance, and the bottom profile on various hydrodynamic characteristics of the transient oscillation are comprehensively investigated. The hydrodynamic characteristics considered include the evolution of the maximum free-surface elevation, the maximum runup, the wave energy distribution and the total wave energy inside the harbor. The results of the current research have enhanced the understanding on the transient harbor resonance triggered by tsunamis.

Based on the research results of this article, some main conclusions are drawn as follows:

- The evolution of the maximum free-surface elevation inside the harbor can be estimated well
  by Green's law, except at the area where the incident and the reflected waves interact with each
  other near the backwall. The valid spatial range of Green's law is intensively dependent on the
  topography and the incident wave height.
- 2. For all the topographies considered, the maximum runups caused by the DSWs with various relative separation distances and the identical wave height are almost identical to each other when the incident wave height is relatively small ( $A_0 \le 0.150$  m). For the incident DSWs have larger wave heights, the maximum runups with R=0.4 gradually becomes larger than those with R=0.6 and 0.8. The impacts of the topography on the maximum runup rely heavily on the incident wave height.
- 3. The wave energy distribution inside the harbor has the trend of becoming more uniform as the

- 1 incident wave height and the relative separation distance increase. In addition, the smaller mean
- 2 water depth can also result in the greater uniformity of the wave energy distribution, no matter
- 3 whether the incident wave height and the relative separation distance are large or small.
- 4. The normalized total wave energy always declines monotonously with the rise of the incident
- 5 wave height. As R rises from 0.4 to 0.6, the normalized total wave energy shows a certain
- 6 degree of decline, while as R grows further from 0.6 to 0.8, the normalized total wave energy
- 7 becomes insensitive to R. The normalized total wave energy is always shown to continuously
- 8 increase first and then slightly decrease with the rise of the mean water depth.
- 9 Finally, we reaffirm here that these conclusions are only valid for the elongated harbor, the
- incident DSWs and the variation ranges of the incident wave height, the relative separation distance,
- and the mean water depth inside the harbor considered in the current study.

# 13 Acknowledgments

12

17

- This research is financially supported by the National Key Research and Development Program
- 15 (2017YFC1404200), the National Natural Science Foundation of China (Grant Nos. 51911530205,
- 16 51809039 and 51609108), and the Royal Society of UK (Grant No. IEC\NSFC\181321).

# 18 References

- 19 Chen, Q., 2006. Fully nonlinear Boussinesq-type equations for waves and currents over porous beds.
- Journal of Engineering Mechanics 132 (2), 220-230.
- 21 Craig, W., Guyenne, P., Hammack, J., Henderson, D., Sulem, C., 2006. Solitary water wave
- interactions. Physics of Fluids 18, 057106.
- De Jong, M.P.C., Holthuijsen, L.H., Battjes, J.A., 2003. Generation of seiches by cold fronts over
- the southern North Sea. Journal of Geophysical Research 108 (C4), 3117,
- 25 doi:3110.1029/2002JC001422.
- Dong, G., Gao, J., Ma, X., Wang, G., Ma, Y., 2013. Numerical study of low-frequency waves during
- harbor resonance. Ocean Engineering 68, 38-46.
- Dong, G., Wang, G., Ma, X., Ma, Y., 2010. Harbor resonance induced by subaerial landslide-
- 29 generated impact waves. Ocean Engineering 37 (10), 927-934.
- Dong, G., Zheng, Z., Gao, J., Ma, X., Dong, Y., Wu, H., 2020a. Experimental investigation on

- special modes with narrow amplification diagrams in harbor oscillations. Coastal
- 2 Engineering 159, 103720.
- 3 Dong, G., Zheng, Z., Ma, X., Huang, X., 2020b. Characteristics of low-frequency oscillations in the
- 4 Hambantota Port during the southwest monsoon. Ocean Engineering 208, 107408.
- 5 Dong, J., Wang, B.-L., Liu, H., 2014. Run-up of non-breaking double solitary waves with equal
- 6 wave heights on a plane beach. Journal of Hydrodynamics 26 (6), 939-950.
- 7 El, G.A., Grimshaw, R.H.J., Tiong, W.K., 2012. Transformation of a shoaling undular bore. Journal
- 8 of Fluid Mechanics 709 (371-395).
- 9 Fabrikant, A.L., 1995. Harbor oscillations generated by shear flow. Journal of Fluid Mechanics 282,
- 10 203-217.
- Gao, J., Ji, C., Gaidai, O., Liu, Y., 2016a. Numerical study of infragravity waves amplification
- during harbor resonance. Ocean Engineering 116, 90-100.
- Gao, J., Ji, C., Gaidai, O., Liu, Y., Ma, X., 2017a. Numerical investigation of transient harbor
- oscillations induced by N-waves. Coastal Engineering 125, 119-131.
- Gao, J., Ji, C., Liu, Y., Gaidai, O., Ma, X., Liu, Z., 2016b. Numerical study on transient harbor
- oscillations induced by solitary waves. Ocean Engineering 126, 467-480.
- Gao, J., Ji, C., Liu, Y., Ma, X., Gaidai, O., 2017b. Influence of offshore topography on the
- amplification of infragravity oscillations within a harbor. Applied Ocean Research 65, 129-
- 19 141.
- 20 Gao, J., Ji, C., Liu, Y., Ma, X., Gaidai, O., 2018a. Numerical study on transient harbor oscillations
- induced by successive solitary waves. Ocean Dynamics 68 (2), 193-209.
- 22 Gao, J., Ji, C., Ma, X., Liu, Y., Gaidai, O., 2017c. Numerical investigation of infragravity wave
- amplifications during harbor oscillations influenced by variable offshore topography.
- 24 Ocean Dynamics 67 (9), 1151-1162.
- Gao, J., Ma, X., Dong, G., Wang, G., Ma, Y., 2015. Improvements on the normal mode
- decomposition method used in harbor resonance. Proc IMechE Part M: Journal of
- Engineering for the Maritime Environment 229 (4), 397-410.
- Gao, J., Ma, X., Dong, G., Wang, G., Ma, Y., 2016c. Numerical study of transient harbor resonance
- induced by solitary waves. Proc IMechE Part M: Journal of Engineering for the Maritime
- 30 Environment 230 (1), 163–176.

- Gao, J., Ma, X., Dong, G., Zang, J., Ma, Y., Zhou, L., 2019a. Effects of offshore fringing reefs on
- the transient harbor resonance excited by solitary waves. Ocean Engineering 190, 106422.
- Gao, J., Ma, X., Dong, G., Zang, J., Zhou, X., Zhou, L., 2019b. Topographic influences on transient
- 4 harbor oscillations excited by N-waves. Ocean Engineering 192, 106548.
- 5 Gao, J., Ma, X., Zang, J., Dong, G., Ma, X., Zhu, Y., Zhou, L., 2020. Numerical investigation of
- 6 harbor oscillations induced by focused transient wave groups. Coastal Engineering 158:
- 7 103670.
- 8 Gao, J., Zhou, X., Zang, J., Chen, Q., Zhou, L., 2018b. Influence of offshore fringing reefs on
- 9 infragravity period oscillations within a harbor. Ocean Engineering, 158: 286-298.
- Gao, J., Zhou, X., Zhou, L., Zang, J., Chen, H., 2019c. Numerical investigation on effects of fringing
- reefs on low-frequency oscillations within a harbor. Ocean Engineering 172: 86-95.
- Gao, J., Zhou, X., Zhou, L., Zang, J., Chen, Q., Ding, H., 2018c. Numerical study of harbor
- oscillations induced by water surface disturbances within harbors of constant depth. Ocean
- Dynamics 68 (12), 1663–1681.
- 15 Grilli, S.T., Harris, J.C., Shi, F., Kirby, J.T., Bakhsh, T.S.T., Estibals, E., Tehranirad, B., 2012.
- Numerical modeling of coastal tsunami impact dissipation and impact, Proceedings of the
- 17 33rd International Coastal Engineering Conference, Santander, Spain.
- Gulshan, Kumar, P., Rajni, 2020. Moored ship motion analysis in Paradip port under the resonance
- conditions using 3-D boundary element method. Journal of Marine Science and Technology.
- 20 https://doi.org/10.1007/s00773-020-00701-0.
- 21 Hayatdavoodi, M., Seiffert, B., Ertekin, R.C., 2014. Experiments and computations of solitary-wave
- forces on a coastal-bridge deck. Part II: Deck with girders. Coastal Engineering 88, 210-
- 23 228.
- 24 Kumar, P., Gulshan, 2017. Extreme wave-induced oscillation in Paradip Port under the resonance
- conditions. Pure and Applied Geophysics 174 (2), 4501-4516.
- Kumar, P., Gulshan, 2018. Theoretical analysis of extreme wave oscillation in Paradip Port using a
- 3-D boundary element method. Ocean Engineering 164, 13-22.
- Kumar, P., Rupali, 2018. Modeling of shallow water waves with variable bathymetry in an irregular
- domain by using hybrid finite element method. Ocean Engineering 165, 386-398.
- Kumar, P., Zhang, H., Kim, K.I., Yuen, D.A., 2016. Modeling wave and spectral characteristics of

- 1 moored ship motion in Pohang New Harbor under the resonance conditions. Ocean
- 2 Engineering 119, 101-113.
- 3 Liu, P.L.-F., Cho, Y.-S., Briggs, M.J., Kanoglu, U., Synolakis, C.E., 1995. Runup of solitary waves
- 4 on a circular island. Journal of Fluid Mechanics 302, 259-285.
- 5 Liu, W., Liu, Y., Zhao, X., 2019. Numerical study of Bragg reflection of regular water waves over
- fringing reefs based on a Boussinesq model. Ocean Engineering 190, 106415.
- 7 Liu, W., Ning, Y., Shi, F., Sun, Z., 2020. A 2DH fully dispersive and weakly nonlinear Boussinesq-
- 8 type model based on a finite-volume and finite-difference TVD-type scheme. Ocean
- 9 Modelling 147, 101559.
- Lo, H.-Y., Park, Y.S., Liu, P.L.-F., 2013. On the run-up and back-wash processes of single and double
- solitary waves An experimental study. Coastal Engineering 80, 1-14.
- Losada, I.J., Gonzalez-Ondina, J.M., Diaz-Hernandez, G., Gonzalez, E.M., 2008. Numerical
- modeling of nonlinear resonance of semi-enclosed water bodies: Description and
- experimental validation. Coastal Engineering 55, 21-34.
- 15 Ma, G., Shi, F., Kirby, J.T., 2012. Shock-capturing non-hydrostatic model for fully dispersive
- surface wave processes. Ocean Modelling 43-44, 22–35.
- Ma, X., Zheng, Z., Zhang, X., Dong, G., 2020. Numerical investigation on special modes with
- narrow amplification diagram in harbor oscillations. Ocean Dynamics 70, 1-19.
- 19 Madsen, P.A., Fuhrman, D.R., Schäffer, H.A., 2008. On the solitary wave paradigm for tsunamis.
- Journal of Geophysical Research: Oceans 113, C12012, doi:10.1029/2008JC004932.
- 21 Madsen, P.A., Schäffer, H.A., 2010. Analytical solutions for tsunami runup on a plane beach single
- waves, N-waves and transient waves. Journal of Fluid Mechanics 645, 27-57.
- 23 Mei, C.C., 1983. The Applied Dynamics of Ocean Surface Waves. Wiley, New York.
- Ning, Y., Liu, W., Sun, Z., Zhao, X., Zhang, Y., 2019a. Parametric study of solitary wave propagation
- and runup over fringing reefs based on a Boussinesq wave model. Journal of Marine
- 26 Science and Technology 24 (2), 512–525.
- Ning, Y., Liu, W., Zhao, X., Zhang, Y., Sun, Z., 2019b. Study of irregular wave run-up over fringing
- reefs based on a shock-capturing Boussinesq model. Applied Ocean Research 84, 216-224.
- 29 Pattiaratchi, C.B., Wijeratne, E.M.S., 2009. Tide gauge observations of 2004-2007 Indian Ocean
- tsunamis from Sri Lanka and Western Australia. Pure and Applied Geophysics 166 (1), 233-

1 258. 2 Rupali, Kumar, P., Rajni, 2020. Spectral boundary element modeling of water waves in Pohang New 3 Harbor and Paradip Port. Ocean Engineering 196, 106765. 4 Seiffert, B., Hayatdavoodi, M., Ertekin, R.C., 2014. Experiments and computations of solitary-wave 5 forces on a coastal-bridge deck. Part I: Flat Plate. Coastal Engineering 88, 194-209. 6 Shi, F., Kirby, J.T., Harris, J.C., Geiman, J.D., Grilli, S.T., 2012. A high-order adaptive time-stepping 7 TVD solver for Boussinesq modeling of breaking waves and coastal inundation. Ocean 8 Modelling 43-44, 36-51. 9 Sobey, R.J., 2006. Normal mode decomposition for identification of storm tide and tsunami hazard. 10 Coastal Engineering 53, 289-301. Synolakis, C.E., 1987. The runup of solitary waves. Journal of Fluid Mechanics 185, 523-545. 11 12 Tadepalli, S., Synolakis, C.E., 1994. The run-up of N-waves on sloping beaches. Proceedings of the Royal Society London A: Mathematical, Physical & Engineering Sciences 445, 99-112. 13 Wang, D., Liu, P.L.-F., 2020. An ISPH with k-ε closure for simulating turbulence under solitary 14 waves. Coastal Engineering 157, 103657. 15